Biomedical Signal Processing and Control 90 (2024) 105851

Contents lists available at ScienceDirect

Biomedical Signal Processing and Control

journal homepage: www.elsevier.com/locate/bspc

Automatic simultaneous ciliary muscle segmentation and biomarker extraction in AS-OCT images using deep learning-based approaches

Elena Goyanes [a,b], Joaquim de Moura [a,b,*], José I. Fernández-Vigo [c,e], José A. Fernández-Vigo [d,e], Jorge Novo [a,b], Marcos Ortega [a,b]

[a] Grupo VARPA, Instituto de Investigación Biomédica de A Coruña (INIBIC), Universidade da Coruña, A Coruña, Spain
[b] Centro de investigación CITIC, Universidade da Coruña, A Coruña, Spain
[c] Department of Ophthalmology, Hospital Clínico San Carlos, Instituto de Investigación Sanitaria (IdISSC), Madrid, Spain
[d] Department of Ophthalmology, Universidad de Extremadura, Badajoz, Spain
[e] Centro Internacional de Oftalmología Avanzada, Madrid, Spain

ARTICLE INFO

Keywords:
CAD system
AS-OCT
Ciliary muscle
Segmentation
Biomarkers
Deep learning

ABSTRACT

Recent clinical studies have emphasized the importance of understanding the morphology and mechanics of the ciliary muscle. The ciliary muscle plays a vital role in various functions related to the anterior segment of the eye, including the regulation of intraocular pressure and the maintenance of the shape of the crystalline lens. To advance research in this area, we propose a fully automated methodology for the segmentation and biomarker measurement of the ciliary muscle in two different scan depths (6 mm and 16 mm), which are commonly used by clinicians to analyze biomarkers. Our methodology aims to provide repeatable, and immediate results through an exhaustive analysis of different network architectures, encoders, and transfer learning strategies. We also extracted a comprehensive set of relevant biomarkers, including parameters that provide essential information about its behavior during the accommodation process, overall dimensions, and biomechanical properties. These biomarkers can help clinicians and researchers in the diagnoses and monitor of different ocular diseases such as glaucoma, myopia, and presbyopia and develop new therapeutic strategies, potentially leading to more effective treatments and improved patient outcomes. Our methodology achieved accurate qualitative and quantitative results, with high accuracy values of 0.9665 ± 0.1280 and 0.9772 ± 0.0873 for the best combinations for 6 mm and 16 mm, respectively. Our proposed system provides a valuable and automatic tool for clinicians and researchers in the segmentation and analysis of the ciliary muscle in AS-OCT images.

1. Introduction

The ciliary muscle is a smooth muscle ring located in the vascular layer of the human eye, responsible for regulating visual accommodation and aqueous humor flow. This control over lens shape is vital for clear vision, allowing the eye to focus on objects at varying distances. Contraction of the ciliary muscle relaxes the zonular fibers attached to the lens, making it more spherical for close-up vision, while relaxation tautens these fibers, flattening the lens for improved distance vision.

Proper ciliary muscle function is indispensable for optimal visual acuity, involving complex physiology influenced by the autonomic nervous system, the sympathetic and parasympathetic systems, and other factors like lens capsule elasticity. Abnormalities or dysfunctions in the ciliary muscle can lead to a range of ocular disorders and visual impairments. Similarly, conditions such as glaucoma and uveitis can lead to changes in the ciliary muscle and affect aqueous humor flow, leading to increased intraocular pressure and vision loss [1–4].

The ciliary muscle is a key structure of the eye, playing an important role in the regulation of accommodation and thus, in our ability to focus on near and distant objects. The morphology and physiology of the ciliary muscle have been studied extensively, and many clinical studies have been developed over the years to investigate its implications in the development and progression of myopia, refractive error, axial ametropia, accommodation, and other related conditions. For instance, Chen et al. [5] reviewed the implications of the ciliary muscle in myopia development and progression, while Baley et al. [6] studied the relation between ciliary body thickness and refractive error in school-age children. Sheppard et al. [7] proposed an analysis of ciliary muscle morphologic changes with accommodation and axial ametropia,

* Corresponding author at: Grupo VARPA, Instituto de Investigación Biomédica de A Coruña (INIBIC), Universidade da Coruña, A Coruña, Spain.
E-mail addresses: elena.goyanes.gonzalez@udc.es (E. Goyanes), joaquim.demoura@udc.es (J.d. Moura), jfvigo@hotmail.com (J.I. Fernández-Vigo), jose.fernandez-vigo@fernandez-vigo.com (J.A. Fernández-Vigo), jnovo@udc.es (J. Novo), mortega@udc.es (M. Ortega).

https://doi.org/10.1016/j.bspc.2023.105851
Received 27 March 2023; Received in revised form 26 October 2023; Accepted 10 December 2023
Available online 20 December 2023

and Lossing et al. [8] measured the changes in ciliary muscle thickness with accommodation in young adults. Moreover, Lewis et al. [9] investigated the morphology of the ciliary muscle during accommodation in a population of children, while Buckhurst et al. [10] analyzed the interrelationships between biometric and morphological characteristics of anterior and posterior segments with reference to temporal and nasal ciliary muscle thickness. Pucker et al. [11] studied the relationship between refractive error and ciliary muscle thickness in different muscle regions, and Kuchen et al. [12] investigated the relationships between ciliary muscle thickness, refractive error, and axial length in adults with anisometropia. Tabernero et al. [13] studied the implication of presbyopia in the ciliary muscle function, finding that it continues working. Wagner et al. [14] provided an in-depth analysis of the morphological changes of the ciliary muscle during accommodation by evaluating ciliary muscle thickness profiles, while their study [15] investigated the accommodation process in emmetropes and myopes regarding morphologic changes of the ciliary muscle and power changes of the lens for different accommodation demands. Fernández-Vigo et al. [16] proposed a study to obtain ciliary muscle measurements and identify correlations in a large population of healthy subjects. Additionally, Shi et al. [17] investigated the cross-sectional area and thickness of the ciliary muscle and their correlation with accommodative lag in hyperopic anisometropic children, while Li et al. [18] evaluated the effects of age on the morphologies of the crystalline lens, ciliary muscle, Schlemm's canal, and trabecular meshwork. Furthermore, Zhang et al. [19] analyzed the morphological characteristics of the ciliary muscle and explored its relationship with different ocular biometric parameters in myopic young Chinese adults, while Kaphle et al. [20] studied the relation between accommodation-induced changes in ciliary muscle dimensions and emmetropes and myopes. Finally, Ren et al. [21] characterized the ciliary body in healthy Chinese subjects, and Anderson et al. [20] analyzed the relationship between ciliary muscle thickness and Down syndrome.

Anterior Segment Optical Coherence Tomography (AS-OCT) imaging has become an indispensable tool for assessing various ocular conditions [22], including the analysis of the ciliary muscle. This non-invasive, real-time, and in vivo imaging technique allows for high-resolution visualization of anterior segment structures. Initially introduced by Izatt et al. in 1994 [23], AS-OCT has since been adopted in the ophthalmic field [24–33]. Its main advantage is the remarkable repeatability and reproducibility for clinically evaluating morphological changes in the anterior segment, including the ciliary muscle.

In addition to its numerous applications, the ciliary muscle's morphological features, as captured by AS-OCT imaging, can serve as valuable biomarkers for various ocular conditions and diseases. These biomarkers have the potential to aid in early diagnosis, monitor disease progression, and evaluate treatment effectiveness [12,15,34–37]. Furthermore, they could provide critical insights into the biomechanical properties of the ciliary muscle, enhancing our understanding of its role in ocular health and disease. By harnessing the potential of these biomarkers, researchers and clinicians can collaborate to develop more targeted and personalized therapeutic approaches, ultimately improving patient outcomes and overall ocular health.

The AS-OCT images produced are cross-sectional scans, which provide an accurate representation of the anatomical structures of the anterior segment. Fig. 1 depicts representative AS-OCT images with the ciliary muscle manually delineated in green. Accurate segmentation of the ciliary muscle from AS-OCT images is essential for analyzing its morphological characteristics.

In recent years, AS-OCT imaging has become a valuable tool for analyzing the ciliary muscle due to its ability to provide high-resolution cross-sectional scans of the anterior segment of the eye in a non-invasive, real-time, and in vivo manner. However, manual segmentation of the ciliary muscle using the software integrated in the OCT device is often time-consuming and requires expertise, making it less efficient and less reproducible. To overcome these limitations, researchers have proposed various semi-automated tools that provide segmentation and measurement of the ciliary muscle. For instance, Kao et al. [38] developed a semi-automatic algorithm for segmentation and morphological assessment of the dimensions of the ciliary muscle, while Ruggeri et al. [39] proposed an algorithm to provide corrected thickness measurements of the ciliary muscle. Laughton et al. [40] designed a software that extracts morphometric data from the ciliary muscle, while Straßer et al. [41] presented a software for semi-automatic segmentation of the ciliary muscle. Although these semi-automated systems have shown promising results, they still require expert intervention, and the results may differ depending on the expertise of the operator.

To address these limitations, a few fully automatic deep learning-based approaches have recently been proposed. Recently, Goyanes et al. [42] published a preliminary study in which they proposed an initial approach for fully automated ciliary muscle segmentation using a deep learning-based algorithm. Their method employs a U-Net architecture to segment the ciliary muscle, achieving high accuracy and efficiency. Similarly, Cabeza et al. [43] developed an automated segmentation tool for transscleral OCT images using Fully Convolutional Networks (FCNs). Straßer & Wagner [44] present a convolutional neural network trained for the automatic segmentation of the ciliary muscle in AS-OCT images. Chen et al. [45] developed an automatic segmentation framework for the ciliary muscle that can be used to analyze the morphological parameters of the ciliary muscle and its dynamic changes during accommodation. These approaches offer a significant improvement in accuracy, reproducibility, and efficiency for researchers and clinicians, providing a standardized and objective analysis of the ciliary muscle, allowing for more reliable diagnosis and monitoring of ocular diseases. Additionally, Wagner et al. [14] and Cabeza et al. [43] extract the ciliary muscle thickness profile to evaluate the morphological changes during accommodation.

Despite the growing and very recent interest in deep learning-based approaches for automated segmentation of the ciliary muscle using AS-OCT images, there is still a significant gap in the state of the art. These methods have not been thoroughly evaluated by clinicians across the most commonly used AS-OCT scan depths, and extracting and evaluating biomarkers from the ciliary muscle remains a challenge due to the difficulties in obtaining labeled images. Therefore, further research is required to develop fully automated methods that can accurately and reproducibly segment and analyze the ciliary muscle across various AS-OCT scan depths while overcoming these challenges.

In this study, we address the existing gap by presenting a fully automated two-step methodology for the segmentation and analysis of the ciliary muscle in AS-OCT images at two commonly used scan depths (6 mm and 16 mm), which are typically employed in daily clinical practice. The proposed methodology comprises two critical steps: ciliary muscle segmentation and extraction of biomarkers. To achieve this, we employ two deep learning-based approaches: U-Net and Feature Pyramid Network (FPN), combined with two different encoders, ResNet-18 and ResNet-34. After exhaustively evaluating these approaches, we select the optimal segmentation model and extract relevant biomarkers for subsequent analysis.

Our proposed system is designed in close collaboration with clinicians and offers the automatic extraction of six significant biomarkers that are commonly measured manually in clinical practice for analysis and diagnostic purposes. These biomarkers include ciliary muscle length (CML), ciliary muscle area (CMA), ciliary muscle thickness measured at 1 mm (CMT1), 2 mm (CMT2), and 3 mm (CMT3) from the scleral spur and complete ciliary muscle thickness profile (CMT profile). These biomarkers allow for a comprehensive evaluation of the ciliary muscle morphology and its behavior during the accommodation process, providing essential information about its overall dimensions and biomechanical properties. Clinicians and researchers can use these biomarkers to help to diagnose and monitor ocular diseases such as glaucoma, myopia, and presbyopia, and develop new therapeutic strategies [10,15,34]. The proposed methodology has the

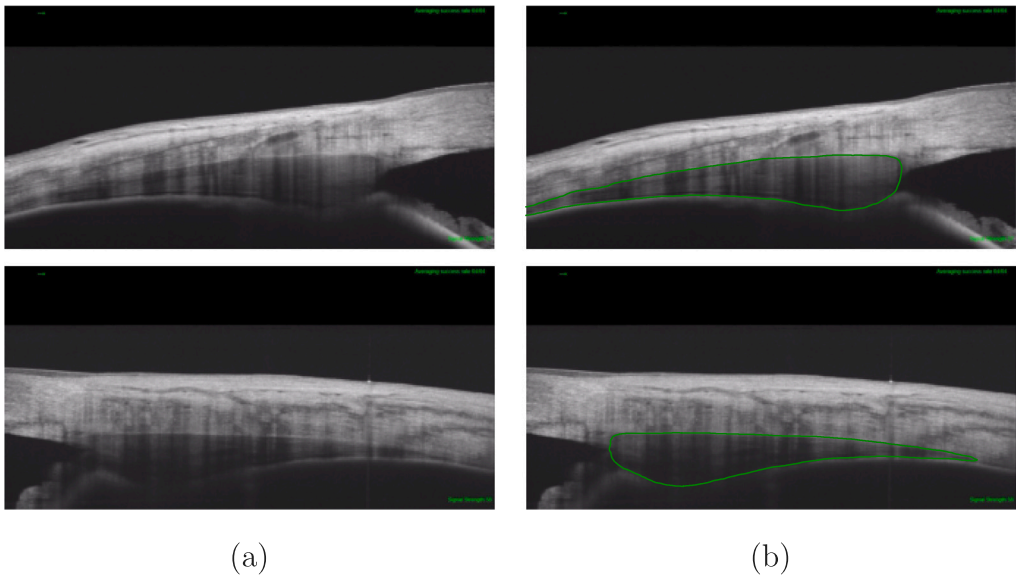

Fig. 1. Illustration of AS-OCT images (a) and the images with the ciliary muscle manually delimited in green (b).

potential to provide clinicians and researchers with a valuable tool for the automated segmentation and analysis of the ciliary muscle in AS-OCT images, offering benefits in ophthalmology research and clinical practice. We outline the main strengths of our proposed methodology as follows:

- First, our fully automated system, developed in close collaboration with clinicians, provides accurate and objective measurements of important biomarkers related to the ciliary muscle. These biomarkers, which are typically calculated by clinicians for their daily practice, can be used to evaluate ciliary muscle morphology and behavior during the accommodation process. This can offer supplementary insights into different ocular conditions. By focusing on the biomarkers that are most relevant to clinical practice, our system ensures that the extracted parameters have direct applicability and value in real-world settings.
- Second, the elimination of manual segmentation and measurements reduces inter- and intra-observer variability and ensures repeatable and instantaneous analysis. This not only improves the reliability and consistency of the measurements but also saves time for clinicians and researchers, simplifying their work. Wagner et al. [14] and Straßer & Wagner [44] provide valuable insights into the importance of the repeatability of biomarkers derived from both semi-automated and fully-automated analysis.
- Finally, our proposed methodology offers a powerful tool for the automated segmentation and analysis of the ciliary muscle in AS-OCT images, providing essential information about its overall dimensions and biomechanical properties. This has the potential to benefit ophthalmology research and clinical practice by helping in the diagnosis and monitoring of ocular diseases such as glaucoma as well as the development of new therapeutic strategies.

Considering these aspects, although some of the techniques we employ might be established, the integration, optimization, and focus on tangible clinical benefits lend our work a distinct value. The potential clinical significance of our research, especially the accurate segmentation of the ciliary muscle in AS-OCT images, hints at profound implications for the ophthalmology field.

To provide a comprehensive understanding of our work, this manuscript is structured as follows: Section 2 provides an overview of the dataset, as well as the software and hardware utilized in the experiments. Section 3 details the proposed methodology, including the network architectures, training procedures, data augmentation techniques, transfer learning, and evaluation criteria. Section 4 presents and discusses the results obtained from the experiments. Finally, Section 5 summarizes the contributions made by this study and highlights the key takeaways from the results.

2. Materials

In this section, we provide comprehensive details regarding the dataset utilized in this study, as well as the software and hardware employed during the research. By thoroughly detailing the dataset and tools utilized, we aim to ensure transparency and reproducibility, thereby enabling other researchers to build upon our work and reproduce the results.

2.1. Dataset

In this study, we utilized a custom dataset specifically designed for our research. The dataset used for the segmentation task contained 1035 AS-OCT images and their corresponding ciliary muscle labels, which were divided into two subsets based on the scan depth of 6 mm and 16 mm, with 931 and 104 images, respectively. Fig. 2 shows the visual differences between the two types of images with an example of each subset, AS-OCT images captured at a shallower depth (6 mm) may exhibit higher resolution and more distinct features of the ciliary muscle, whereas those at a deeper depth (16 mm) might provide a broader view of the internal structures, albeit with lesser detail. In addition, a dataset comprising of 732 images with a scan width of 6 mm was employed to evaluate the performance of our automated biomarker extraction approach. In close collaboration with clinical experts, our approach has been designed to automatically extract five key biomarkers that are typically measured manually in clinical practice. These biomarkers include ciliary muscle length (CML), ciliary muscle area (CMA), and ciliary muscle thickness measured at 1 mm (CMT1), 2 mm (CMT2), and 3 mm (CMT3) from the scleral spur. Complementary, we extract the complete ciliary muscle profile. By aligning our methodology with the needs and expertise of clinicians, we ensure that the extracted biomarkers are highly relevant and valuable for the analysis and diagnosis of ocular conditions, facilitating the adoption of our automated system in real-world clinical settings.

All the AS-OCT images were acquired as part of a cross-sectional study conducted at the International Centre for Advanced Ophthalmology in Madrid, Spain. The study recruited healthy subjects who

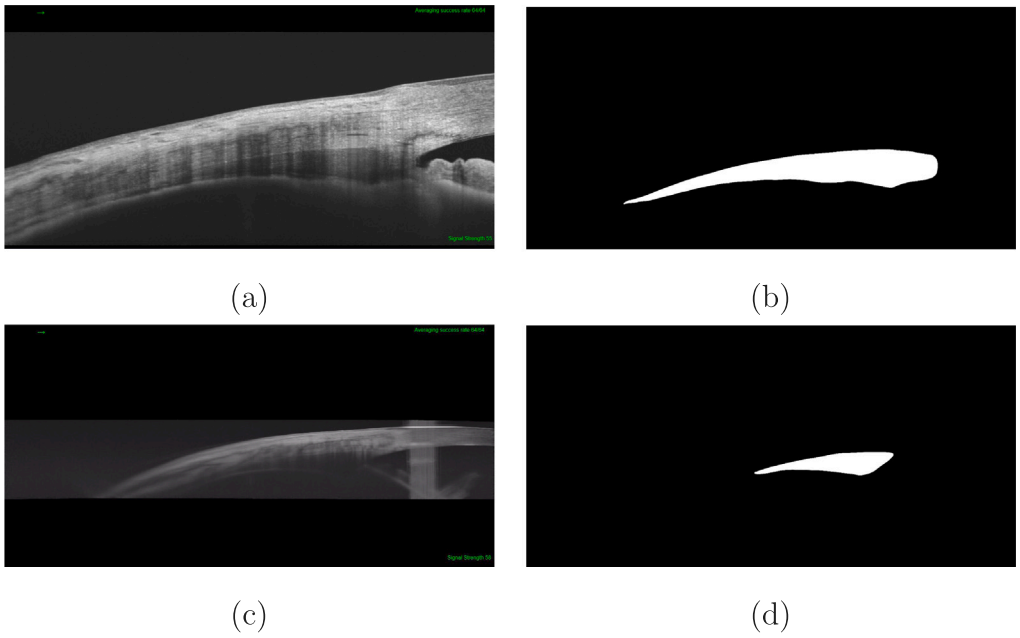

Fig. 2. Example of AS-OCT images (1*st* column) and its corresponding ciliary muscle manually labeled (2*nd* column) with a scan width of (a, b) 6 mm and (c, d) 16 mm.

underwent routine eye examination between 1 February 2018 and 21 January 2019. The eligible patients were of Caucasian descent with a spherical refractive error between −6 to +6 diopters, had no previous ocular pathology found in the examination, an intraocular pressure of (IOP) <= 21 mmHg, and had no previous ocular surgery. The study protocol adhered to the tenets of the Declaration of Helsinki and was approved by the Center's Review Board. Patients who gave their informed consent underwent a medical history and a complete ophthalmologic examination followed by SS-OCT, which included visual acuity and cycloplegic refractive error, slit-lamp biomicroscopy, tonometry with Canon TX 10® pneumotonometer (Canon Inc.; Tokyo, Japan), and posterior segment ophthalmoscopy. The SS-OCT CM analyses were conducted using the DRI-Triton® device by Topcon Corporation, Tokyo, Japan. This equipment operates with a central wavelength of 1050 nm and possesses an axial resolution of 8 μm and a lateral resolution of 20 μm, performing 100,000 A-scans per second.

The OCT images were captured prior to pupil dilation, with scans administered by a proficient examiner while the subjects were seated upright. Participants were guided to maintain either maximum temporal or nasal gaze during scans to facilitate precise examination of the ciliary body at the 3- and 9-o'clock positions. To assure stable fixation throughout the scan, we used an auxiliary fixation light. The fixation point was determined with a goniometer, marked 60º from the central axis of the device and approximately 60 cm distant, ensuring subjects' chin and forehead were securely positioned to avoid movement during the procedure.

Inclusion of images was contingent on obtaining a sufficient quality threshold, with a Signal Strength Intensity (SSI) exceeding 40. OCT scans were carried out under uniform mesopic lighting conditions, set at 7 EV or 320 lux, as verified by a SEKONIC Flash mate K-308S® lightmeter.

To acquire cross-sectional images of the ciliary body, the anterior segment lens of the device was used, applying the 6-mm and 16-mm "line" capture modes. The CM was visualized as a hyporeflective triangular structure, discerned by distinctive layers and interfaces. Detailed measurements of different aspects of the ciliary body were obtained, including the length, area, and thickness at specified points, and incorporated additional evaluations like the anterior chamber angle and iris thickness at a particular distance from the scleral spur in the captured OCT images. The images were exported in the JPEG (Joint Photographic Experts Group) format. We aimed to maintain a high-quality representation of the original data while ensuring the accessibility and compatibility of the images with our processing and analysis tools.

2.2. Software and hardware

This research utilized Python (version 3.9.9) as the primary programming language to write all the code. We used PyTorch (version 1.8.1), an open-source machine learning framework, for the training and validation of the models. The Segmentation Models PyTorch library [46] was utilized in our methodology to train and evaluate different models and encoders for ciliary muscle segmentation. This library provides a wide range of popular and state-of-the-art segmentation models and encoders that can be easily adapted and fine-tuned for different applications. For image processing purposes, we used OpenCV (version 4.5.2), an open-source computer vision library. The models were trained, validated, and tested on a computer (Intel® Xeon® CPU E5-2640 v3 @ 2.60 GHz) with an NVIDIA® GeForce GTX TITAN X GPU.

3. Methodology

In this section, we provide a detailed description of the methodology employed in this study. As shown in Fig. 3, the proposed system is designed to take an AS-OCT image as input and perform ciliary muscle segmentation, followed by automatic extraction of biomarkers from the segmented image. The resulting output is the original input image with all the biomarkers depicted, along with their respective measurements for easy readability. The following subsections provide more detailed information on the different components of the methodology, including the network architecture and encoder configurations used for ciliary muscle segmentation, as well as the automated biomarker extraction approach.

3.1. Ciliary muscle segmentation

The accurate segmentation of the ciliary muscle is essential for the automated analysis of AS-OCT images. To achieve this, we employed two popular network architectures, U-Net and FPN, combined with two different encoders, ResNet-18 and ResNet-34, to compare their

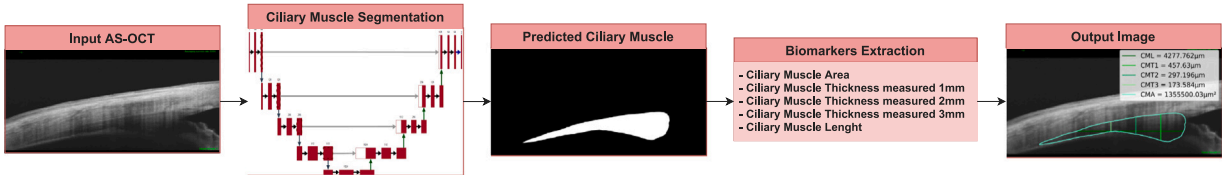

Fig. 3. General scheme of the methodology.

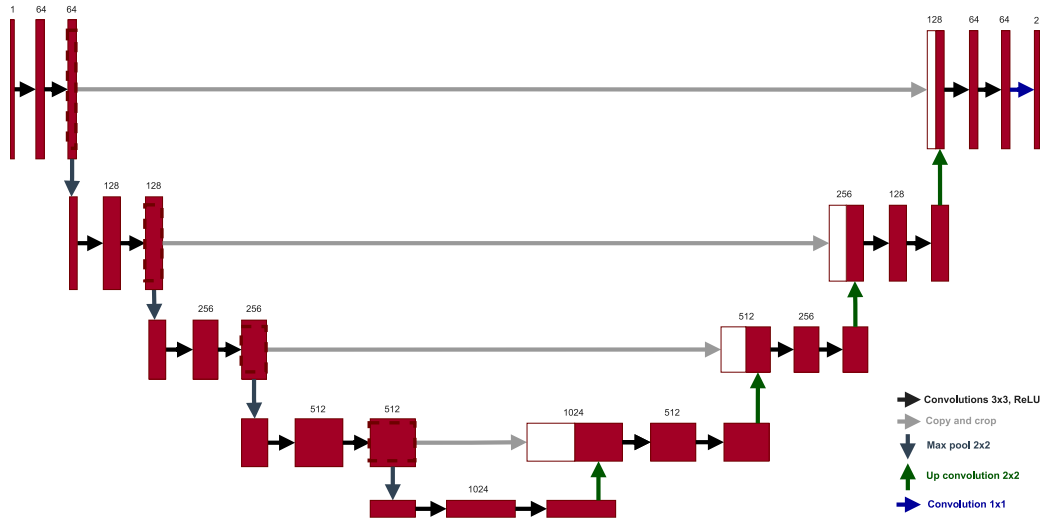

Fig. 4. Architecture diagram of the U-Net network used in our study.

performance and determine which architecture produces better results. U-Net was selected as the reference architecture for semantic segmentation tasks in medical images due to its ability to accurately segment complex structures. FPN was chosen because it uses a pyramidal analysis paradigm at different scales, which can be beneficial for solving this problem. These network architectures have been widely used in medical image segmentation tasks and have demonstrated the ability to accurately identify complex structures and objects within images. By evaluating these architectures in our study, we aimed to determine the optimal approach for ciliary muscle segmentation in AS-OCT images.

3.1.1. Network architecture

The U-Net architecture, developed by Ronneberger et al. [47], is a fully convolutional network that achieves precise segmentation while requiring only a small number of training images. It is commonly used in biomedical imaging related tasks and is selected as the reference architecture for semantic segmentation tasks in medical imaging. The U-Net architecture consists of a set of operations that reduce the resolution of the input (known as the "shrinkage path") on the left side of the network. The right side of the network (known as the "expansion path") consists of blocks that recover the original resolution of the input. Fig. 4 illustrates the U-Net network architecture. Further details of its components could be found in [47].

The Feature Pyramid Network (FPN) is a fully convolutional network architecture proposed by Lin et al. [48]. FPN is designed to address the problem of scale variance that commonly occurs in object detection tasks in computer vision [49]. In the context of our work, the ciliary muscle and surrounding structures in AS-OCT images can exhibit variations in size, shape, and resolution, making the use of FPN particularly relevant for our application. This architecture uses a pyramidal analysis paradigm at different scales, allowing the network to learn representations that are invariant to scale. In particular, FPN consists of two pathways, a bottom-up and a top-down pathway. Fig. 5 displays the structure of the FPN network architecture that is explained in detail in [48].

3.1.2. Encoder configurations

The encoder plays a crucial role in the performance of a network for medical image segmentation. Encoders with more parameters and depth typically perform better by extracting more complex and high-level features. However, too many parameters and depth can lead to overfitting and longer training times. Therefore, a balance must be found between the encoder's parameters and depth and the network's performance. In this work, we analyzed the performance of the U-Net and FPN architectures with two encoders: ResNet-18 and ResNet-34. These encoders were chosen because of their proven effectiveness in various medical image analysis tasks [50–55]. The aim of our study was to identify the best combination of network architecture and encoder to achieve accurate and robust segmentation of the ciliary muscle in AS-OCT images.

Our proposed approach utilizes two encoders based on the Residual Neural Convolutional Network [56], which utilizes skip connections to add the input of a layer to the output of a deeper one. Specifically, we use the ResNet-18 encoder, which consists of 18 parameter layers and approximately 11 million parameters, and the ResNet-34 encoder, which consists of 34 parameter layers and approximately 63 million parameters. It is worth noting that the ResNet-34 encoder has more than five times the number of parameters of the ResNet-18 encoder.

Using these two different encoders allows us to analyze the behavior of the U-Net and FPN architectures with different numbers of parameters and depths. The ResNet-18 encoder provides a simpler and faster alternative to the ResNet-34 encoder with fewer parameters and lower depth, while the ResNet-34 encoder can extract more complex and high-level features due to its higher depth and greater number of parameters.

3.1.3. Training details

We have trained and evaluated the models independently for the two distinct datasets corresponding to the two scan depths of 6 mm and 16 mm in order to facilitate the assimilation and adaptation to the specific characteristics and details intrinsic to each scan depth.

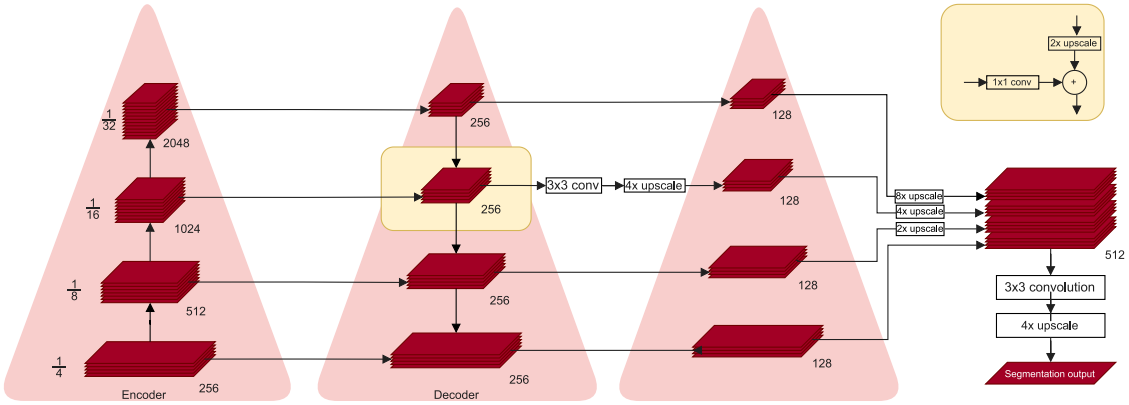

Fig. 5. Architecture diagram of the FPN network used in our study.

To ensure the robustness and reliability of our training process, we repeated the training task five times and computed the mean and standard deviation of the statistics. In each repetition, we randomly divided the dataset into three smaller subsets: training, validation, and testing, with 60%, 20%, and 20% of the cases for each subset, respectively. Only one image per eye was taken for the study. Therefore, we have ensured that images from a single eye are exclusively assigned to one data set, avoiding any splits between the training, validation and testing data sets. The training set was used to optimize the network's parameters, the validation set was used to monitor the training process and avoid overfitting, and the testing set was used to evaluate the final performance of the trained model. By doing the five random divisions of the data set, we aimed to ensure that the results obtained are a true representation of the inherent capabilities of the model and are not merely a byproduct of favorable initial conditions or specific arrangements of the data during training, thereby providing a more comprehensive and robust understanding of its capabilities, resilience, and reliability.

To adjust the network weights and biases, we used the Adam optimization algorithm [57] with a learning rate of 0.0001. The Adam algorithm is a popular optimization technique for deep learning models that combines the advantages of two other optimization algorithms, namely, adaptive gradient algorithm and root mean square propagation.

To conduct the training, we used the Dice loss ($\mathcal{L}DSC$), which is a commonly used loss function in the field of biomedical image segmentation. The Dice loss is defined in Eq. (2), where $p_{i,c}$ represents a matrix of predicted values generated by the model for each class, and $y_{i,c}$ uses a one-hot encoding scheme corresponding to the ground truth labels. Here, i and c represent indices that iterate over all pixels and classes, respectively.

$$\mathcal{L}_{DSC} = 1 - \frac{1}{C}\sum_{c=1}^{C}\frac{2\sum_{i=1}^{N} p_{i,c}y_{i,c}}{\sum_{i=1}^{N} p_{i,c} + \sum_{i=1}^{N} y_{i,c}} \tag{1}$$

The $\mathcal{L}DSC$ measures the overlap between the predicted and ground truth segmentation masks, and aims to maximize the similarity between the two masks. During the training process, the loss is minimized by adjusting the network parameters using the Adam optimizer.

3.1.4. Data augmentation

In this work, we implemented a data augmentation strategy to increase the size of our training dataset and address the overfitting issue caused by the limited amount of available data. This strategy involved applying various computer vision techniques to the AS-OCT images in the training set after the initial partitioning, generating new training samples that better capture the inherent variability of real-world data and ensuring that new samples derived from the same source are all in the training set, preventing contamination between the different sets.

Specifically, we employed a combination of affine transformations, including horizontal flips with a 0.5 probability, scaling with a factor between 0.5 and 1.5, and translation with a 0.1 factor. Additionally, we introduced random variations in brightness and contrast with a 0.9 probability and a 0.2 factor range, applied a Gaussian filter using a randomly sized kernel and a variance range for noise between 10 and 50 with a 0.2 probability, and incorporated blur, motion blur, and sharpening techniques. These methods were used with a random kernel size, a limit of 3, and a 0.3 probability, with sharpened images being overlaid on the original images. Similar augmentation techniques are used in other relevant works of the state of the art [41,44].

Data augmentation is a widely utilized technique in deep learning, known for its ability to enhance model performance and generalization by increasing the diversity of the training data. By incorporating these various transformations, we successfully generated new training samples that better represent the variability found in real-world data, ultimately improving the robustness and reliability of our models maintaining a strict separation between the training, validation and test sets.

3.1.5. Transfer learning

The transfer learning technique consists of training a model using images from a large dataset before fine-tuning it with a specific dataset. This technique helps to mitigate the lack of training data that is still present in many biomedical fields, where acquiring large and annotated datasets is a challenging task. Transfer learning has shown promising results in such scenarios and is widely used in computer vision applications.

In this work, we evaluate the effect of transfer learning by training the same models from scratch and then using models pre-trained on ImageNet [58], a large image dataset that contains more than 1.5 million annotated images across 1000 classes. We use these pre-trained models as initial weights for fine-tuning our models on the AS-OCT images dataset. By doing so, we leverage the pre-existing knowledge of the pre-trained models to extract useful features from the AS-OCT images and enable the models to achieve better performance with a smaller training dataset.

3.1.6. Evaluation of ciliary muscle segmentation

Precision, Recall, Accuracy, Jaccard and Dice coefficient (Eqs. (2), (3), (4), (5) & (6), respectively), are the most commonly used statistical metrics in the state of the art [59,60] to quantitatively evaluate and validate the ciliary muscle segmentation developed by our method. These metrics are used to compare the predicted segmentation with the ground truth labels.

$$\text{Precision} = \frac{TP}{TP + FP} \tag{2}$$

$$\text{Recall} = \frac{TP}{TP + FN} \tag{3}$$

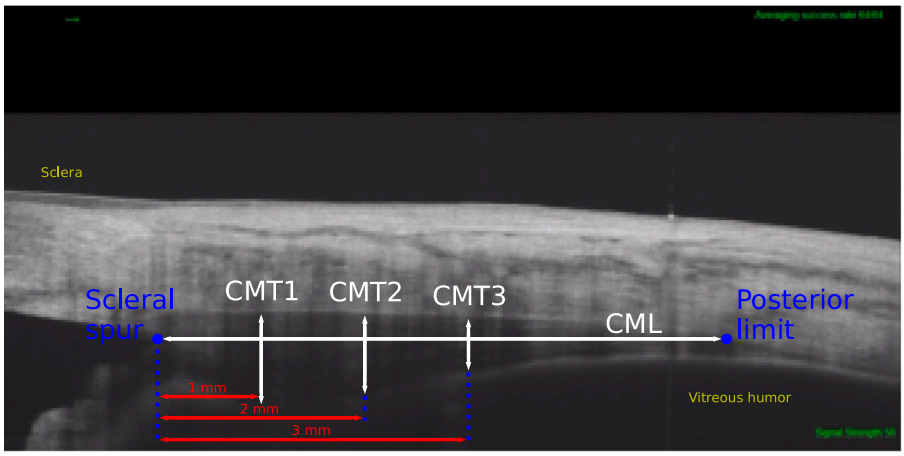

Fig. 6. Illustrative representation of the key biomarkers automatically extracted from AS-OCT images, including ciliary muscle length (CML), and thickness measurements at 1 mm, 2 mm, and 3 mm from the scleral spur (CMT1, CMT2 and CMT3, respectively).

$$\text{Accuracy} = \frac{TP+TN}{TP+TN+FP+FN} \tag{4}$$

$$\text{Jaccard} = \frac{TP}{TP+FP+FN} \tag{5}$$

$$\text{Dice} = \frac{2\times TP}{2\times TP+FP+FN} \tag{6}$$

TP, TN, FP and FN depict the number of True Positives, True Negatives, False Positives and False Negatives, respectively, and are computed based on the predicted and target labels.

3.2. Automatic extraction of biomarkers

The extraction of biomarkers is an essential step in medical image analysis, as it enables clinicians and researchers to obtain quantitative measurements and insights that can aid in diagnosis and treatment planning. In the context of ciliary muscle segmentation, the automatic extraction of biomarkers can provide valuable information on the morphology and behavior of the ciliary muscle during the accommodation process, as well as its relation to various pathologies [6–12,14–21,61–63].

In this work, we propose an approach for the automatic extraction of five biomarkers of high clinical importance in ciliary muscle segmentation, developed in close collaboration with clinical experts: Ciliary Muscle Length (CML), Ciliary Muscle Area (CMA), and Ciliary Muscle Thickness measured at 1 mm (CMT1), 2 mm (CMT2), and 3 mm (CMT3) from the scleral spur. These biomarkers are typically calculated manually by clinicians and can be extracted automatically using a deep learning-based method trained on AS-OCT images. Fig. 6 shows an illustrative representation of how these biomarkers are measured. Furthermore, we export the complete Ciliary Muscle Thickness Profile (CMT profile).

CML represents the length of the ciliary muscle, which is calculated as the maximum width of the muscle, determining the widths at all heights of the muscle in a straight line. It is expressed in micrometers (μm). The Posterior Limit is defined as the point on the border of the ciliary muscle at the height where the muscle has the maximum width. CMA, on the other hand, represents the area of the ciliary muscle that can be seen in the images, and is also calculated in micrometers squared (μm^2).

CMT1, CMT2, and CMT3 represent the thickness of the ciliary muscle measured at 1 mm, 2 mm, and 3 mm from the scleral spur, respectively. These biomarkers are calculated as the vertical distance between the top and bottom borders of the ciliary muscle at the specified distances from the scleral spur. They are also expressed in micrometers. We also represent the complete ciliary muscle thickness profile (CMT profile), offering an overall view of the thickness of the ciliary muscle, with the value of the perimeter of the profile as quantitative measurement.

Our proposed system is designed to work with the two most common scan depths (6 mm and 16 mm) used in clinical practice, ensuring that the methodology is realistic and applicable to a wide range of clinical scenarios. The automatic extraction of these biomarkers using our proposed approach can provide clinicians and researchers with valuable insights into the ciliary muscle, enabling better understanding and diagnosis of various ocular conditions.

3.2.1. Evaluation of the biomarkers

To ensure the reliability and accuracy of the automatic extraction of the different biomarkers, we conducted a comprehensive evaluation of our approach using various statistical metrics and qualitative analysis techniques. To quantitatively evaluate the extraction of the CMT profiles, we calculate the perimeter of both, the CMT profile and the ground truth, comparing these values.

We used a box plot and a Bland–Altman analysis to compare the measurements calculated by a clinical expert and those calculated by our approach, in order to assess the differences between them. The box plot provides a visual representation of the distribution of measurements for each biomarker, allowing us to observe any potential outliers and compare the ranges of values. The Bland–Altman analysis, on the other hand, allows us to assess the agreement between the measurements obtained by the two methods by plotting the difference between the two measurements against their average. This analysis helps us identify any systematic biases or limits of agreement between the two methods and it is commonly used to evaluate similar tasks [64–67]. Specifically, the Bland–Altman analysis calculates the mean difference (bias) between the two methods using Eq. (7):

$$\text{bias} = \frac{1}{n}\sum_{i=1}^{n}(x_i - y_i) \tag{7}$$

where x_i represent the measurements obtained by the clinical expert and y_i the ones obtained by our approach. We also calculate the 95% limits of agreement (LoA), which are defined as the mean difference between the two methods ± 1.96 times the standard deviation of the differences. In order to calculate the differences, our approach results have been subtracted from the expert calculations.

By presenting strong agreement between our approach and the expert's measurements through these evaluation techniques, we can emphasize the potential of our automated system as a valuable tool for extracting clinically meaningful biomarkers from AS-OCT images. This comprehensive evaluation reinforces the reliability, accuracy, and clinical applicability of our proposed methodology.

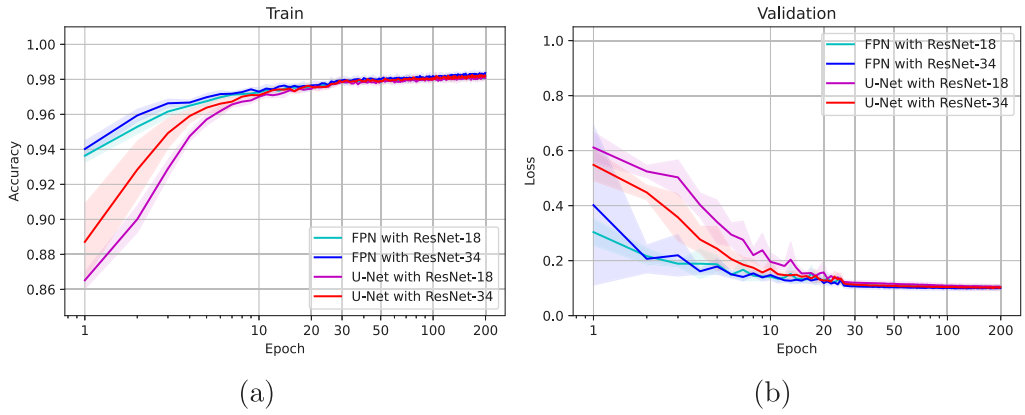

Fig. 7. Evolution of the two architectures (U-Net and FPN) combined with the two encoders (ResNet-18 and ResNet-34) from Scratch in terms of Mean ± standard deviation for the 5 randomized repetitions for the 6 mm images. (a) Training accuracy. (b) Validation loss. Results are presented using a logarithmic scale to a better representation of the results due to the importance of the changes on the first epochs.

4. Results and discussion

In this section, we present the results and discussion of the experiments conducted to evaluate the performance of our approach for the automated segmentation of the ciliary muscle in anterior segment optical coherence tomography (AS-OCT) images and the extraction of different biomarkers. Firstly, we analyze the segmentation performance on two types of AS-OCT images with a depth of 6 mm and 16 mm, respectively, which are commonly used by clinicians to analyze the biomarkers of the ciliary muscle. Secondly, we present the results of the extraction of biomarkers and their evaluation metrics. These metrics are essential for clinical practice and research in understanding the morphology and behavior of the ciliary muscle during the accommodation process and investigating the relationship between the ciliary muscle and various pathologies.

4.1. Performance of ciliary muscle segmentation

In the following subsections, we present the results of the automated segmentation of the ciliary muscle in AS-OCT images using the different neural network configurations developed in this study. Specifically, we analyze the performance of the networks for images with a depth of 6 mm and 16 mm, which are commonly used by clinicians to analyze biomarkers of the ciliary muscle. For each type of image, the networks were trained and validated for 200 epochs, and we established this number of epochs based on the observation that further training did not result in any improvement in accuracy or the $\mathcal{L}_{DSC}$ function. Each experiment was repeated five times using a random seed to ensure the statistical significance of the results.

4.1.1. Performance of ciliary muscle segmentation in 6 mm images

The training accuracy and validation loss evolution of the networks are presented in Figs. 7 and 8, respectively, considering 5 random repetitions for the networks trained from scratch and using transfer learning strategy. As expected, the networks that use transfer learning achieve better accuracy values in the early epochs and reach stability earlier compared to the networks trained from scratch.

Overall, all the neural network configurations perform well for the automated segmentation of the ciliary muscle in AS-OCT images, achieving stability before epoch 30 in terms of mean and standard deviation. The stability of the standard deviation across different configurations highlights the robustness of our approach, which is a highly desirable feature in a clinical setting. The test results for the reference metrics are presented in Table 1, with the U-Net and ResNet-34 encoder using transfer learning achieving the highest values of 0.9665 ± 0.1280, 0.8194 ± 0.1306, 0.8923 ± 0.1194, 0.9109 ± 0.0690, and 0.8969 ± 0.1364 for Accuracy, Jaccard, Dice, Precision, and Recall, respectively.

Moreover, to complement the quantitative evaluation, we present the qualitative results of the automated segmentation in Fig. 9, which displays two representative examples of the ciliary muscle segmentation results obtained from 6 mm AS-OCT images. The resulting segmented image is overlaid on the input image and the manual label to provide a clear visualization of the segmentation performance. As can be observed from the figure, the proposed methodology achieves accurate and consistent segmentation of the ciliary muscle, demonstrating the effectiveness of our approach in providing reliable and objective measurements. These qualitative results further support the potential of our methodology to serve as a valuable tool for the automated segmentation and analysis of ciliary muscle in AS-OCT images for ophthalmology research and clinical practice.

4.1.2. Performance of ciliary muscle segmentation in 16 mm images

In this subsection, we evaluate the performance of our approach for ciliary muscle segmentation in 16 mm AS-OCT images. We analyze the performance of the neural networks trained from scratch and using transfer learning and present the evaluation metrics for the reference standards. Additionally, we discuss the strengths and limitations of our approach based on the obtained results.

The training accuracy and validation loss evolution of the networks are depicted in Figs. 10 and 11, respectively, considering 5 random repetitions for the networks trained from scratch and using transfer learning. As expected, networks that were previously trained obtain better values in the first epochs and achieve stability earlier than the ones trained from scratch. Additionally, it is important to note that compared to the 6 mm images, the training accuracy and validation loss graphs for the 16 mm images show slightly less stability in the validation, which can be attributed to the smaller size of this dataset.

In terms of mean and standard deviation, all neural network configurations achieved satisfactory results for ciliary muscle segmentation in AS-OCT images before epoch 30. The test results for the reference metrics are presented in Table 2, with the FPN architecture using ResNet-34 encoder and transfer learning approach achieving the best performance, with the highest values of 0.9772 ± 0.0873, 0.7326 ± 0.1215, 0.8362 ± 0.1101, 0.8787 ± 0.0890, and 0.8273 ± 0.1373 for Accuracy, Jaccard, Dice, Precision, and Recall, respectively. This stability, combined with the high performance of our proposed method, reinforces the robustness and reliability of our approach, making it suitable for use in a clinical environment where consistent and accurate results are essential.

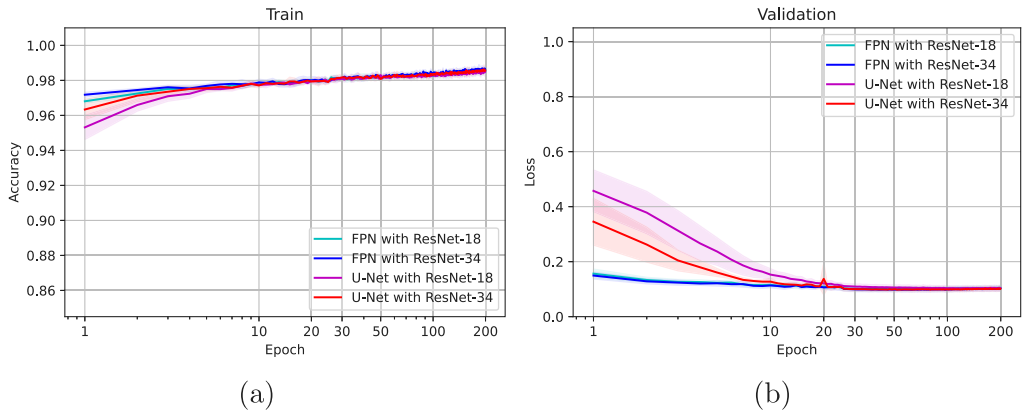

Fig. 8. Evolution of the two architectures (U-Net and FPN) combined with the two encoders (ResNet-18 and ResNet-34) with transfer learning in terms of Mean ± standard deviation for the 5 randomized repetitions for the 6 mm images. (a) Training accuracy. (b) Validation loss. Results are presented using a logarithmic scale to a better representation of the results due to the importance of the changes on the first epochs.

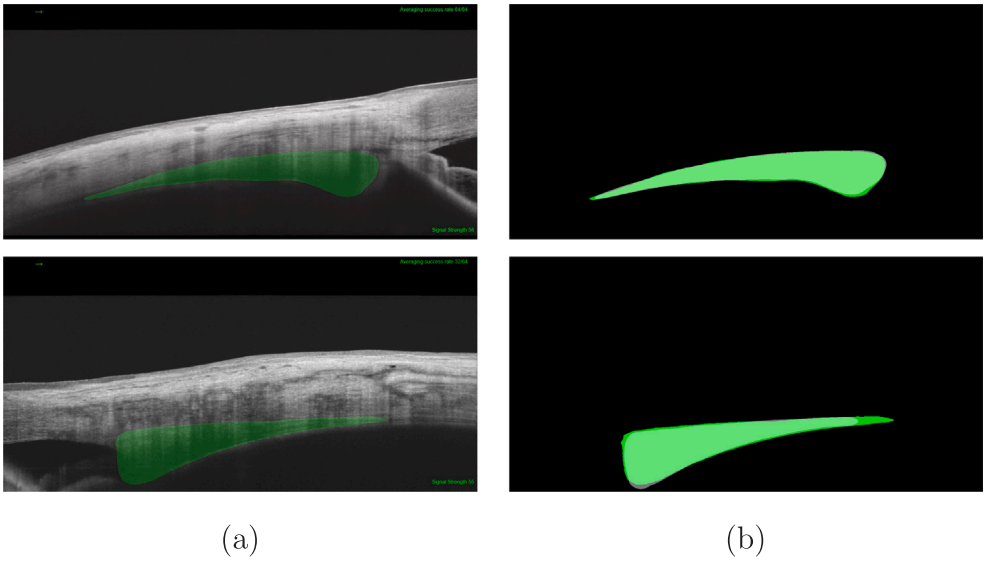

Fig. 9. Examples of the resulting segmented regions (green) in 6 mm images overlapped with: (a) the input image and (b) the manual label provided by a clinical expert (gray).

Table 1
Test results in terms of mean ± standard deviation for the 5 randomized repetitions for the 6 mm images.

Architecture	Encoder	Transfer learning	Accuracy	Jaccard	Dice	Precision	Recall
U-Net	ResNet-18		0.9657 ± 0.1278	0.8106 ± 0.1320	0.8867 ± 0.1200	0.9032 ± 0.0725	0.8937 ± 0.1378
U-Net	ResNet-34		0.9662 ± 0.1278	0.8150 ± 0.1332	0.8891 ± 0.1219	0.9089 ± 0.0724	0.8930 ± 0.1411
U-Net	ResNet-18	•	0.9662 ± 0.1277	0.8151 ± 0.1313	0.8895 ± 0.1197	0.9081 ± 0.0695	0.8943 ± 0.1386
U-Net	ResNet-34	•	0.9665 ± 0.1280	0.8194 ± 0.1306	0.8923 ± 0.1194	0.9109 ± 0.0690	0.8969 ± 0.1364
FPN	ResNet-18		0.9660 ± 0.1279	0.8136 ± 0.1299	0.8887 ± 0.1190	0.9066 ± 0.0700	0.8938 ± 0.1361
FPN	ResNet-34		0.9663 ± 0.1279	0.8170 ± 0.1323	0.8906 ± 0.1207	0.9109 ± 0.0711	0.8940 ± 0.1383
FPN	ResNet-18	•	0.9661 ± 0.1277	0.8148 ± 0.1303	0.8895 ± 0.1189	0.9102 ± 0.0709	0.8916 ± 0.1351
FPN	ResNet-34	•	0.9640 ± 0.1352	0.8183 ± 0.1338	0.8907 ± 0.1248	0.9060 ± 0.0852	0.8983 ± 0.1403

Table 2
Test results in terms of mean ± standard deviation for the 5 randomized repetitions for the 16 mm images.

Architecture	Encoder	Transfer learning	Accuracy	Jaccard	Dice	Precision	Recall
U-Net	ResNet-18		0.9508 ± 0.2086	0.6411 ± 0.2053	0.7492 ± 0.2198	0.8325 ± 0.1858	0.7340 ± 0.2395
U-Net	ResNet-34		0.9586 ± 0.1680	0.6120 ± 0.2190	0.7240 ± 0.2289	0.8164 ± 0.1854	0.7285 ± 0.2573
U-Net	ResNet-18	•	0.9604 ± 0.1677	0.7119 ± 0.1613	0.8133 ± 0.1599	0.8485 ± 0.1680	0.8015 ± 0.1797
U-Net	ResNet-34	•	0.9521 ± 0.2091	0.7131 ± 0.1740	0.8110 ± 0.1850	0.8544 ± 0.1879	0.7928 ± 0.1931
FPN	ResNet-18		0.9758 ± 0.0883	0.6546 ± 0.1973	0.7653 ± 0.1976	0.8541 ± 0.1067	0.7647 ± 0.2330
FPN	ResNet-34		0.9759 ± 0.0877	0.6544 ± 0.1985	0.7632 ± 0.2070	0.8619 ± 0.1062	0.7554 ± 0.2336
FPN	ResNet-18	•	0.9767 ± 0.0875	0.7049 ± 0.1332	0.8146 ± 0.1199	0.8808 ± 0.0963	0.7885 ± 0.1467
FPN	ResNet-34	•	0.9772 ± 0.0873	0.7326 ± 0.1215	0.8362 ± 0.1101	0.8787 ± 0.0890	0.8273 ± 0.1373

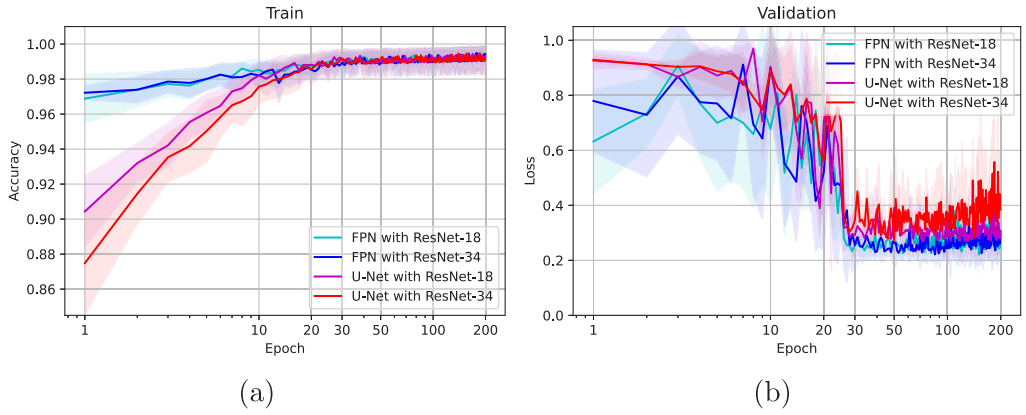

Fig. 10. Evolution of the two architectures (U-Net and FPN) combined with the two encoders (ResNet-18 and ResNet-34) from Scratch in terms of Mean ± standard deviation for the 5 randomized repetitions for the 16 mm images. (a) Training accuracy. (b) Validation loss. Results are presented using a logarithmic scale to a better representation of the results due to the importance of the changes on the first epochs.

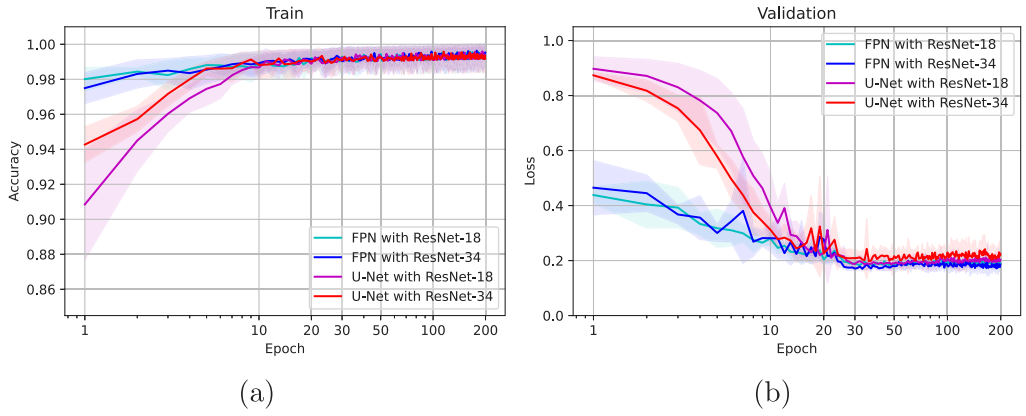

Fig. 11. Evolution of the two architectures (U-Net and FPN) combined with the two encoders (ResNet-18 and ResNet-34) with transfer learning in terms of Mean ± standard deviation for the 5 randomized repetitions for the 16 mm images. (a) Training accuracy. (b) Validation loss. Results are presented using a logarithmic scale to a better representation of the results due to the importance of the changes on the first epochs.

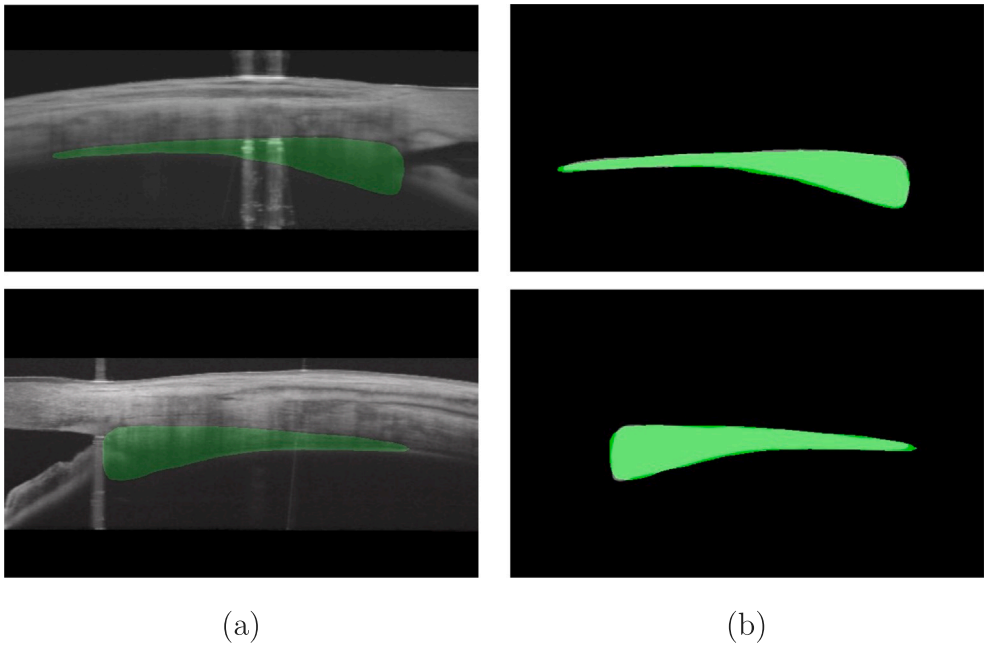

Fig. 12. Cropped examples of the resulting segmented regions (green) in 16 mm images overlapped with: (a) the input image and (b) the manual label provided by a clinical expert (gray).

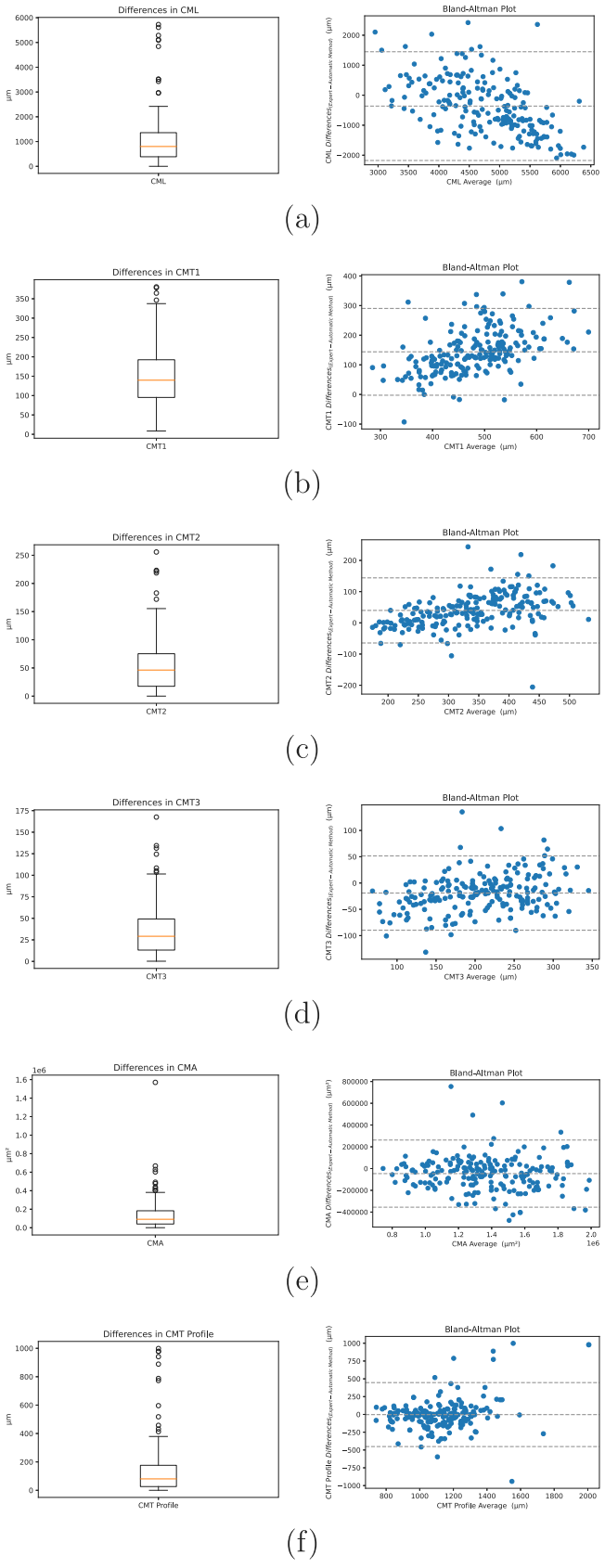

Fig. 13. Box plot and Bland–Altman analysis showing the differences (Expert - Our method) in the biomarkers measurements: (a) CML, (b) CMT1, (c) CMT2, (d) CMT3, (e) CMA, and (f) CMT profile.

To further demonstrate the effectiveness of our approach, we present two representative examples of the automated segmentation results obtained from 16 mm AS-OCT images in Fig. 12. The resulting segmented images are overlaid on the input images and manual labels provided by clinical experts, highlighting the accuracy and reliability of our approach in segmenting the ciliary muscle. These results suggest that our approach is capable of providing reliable and accurate segmentation of the ciliary muscle in AS-OCT images, commonly used by clinicians to analyze biomarkers related to the ciliary muscle morphology and behavior during the accommodation process.

4.2. Results of the automatic extraction of biomarkers

In this subsection, we report on the results of our proposed approach for the automatic extraction of biomarkers in AS-OCT images of the ciliary muscle. Both qualitative and quantitative analyses of the achieved results are presented.

It is important to emphasize that the automatically extracted biomarker measurements are compared to the manual measurements provided by clinical experts. This comparison serves as a crucial validation step, ensuring that our method produces reliable and accurate results that are consistent with the expert assessments.

In Fig. 13, we provide a quantitative analysis of the results through box plots and Bland–Altman analyses comparing the automatic measurements and those provided by clinical experts for each biomarker. Overall, the results from the box plots and Bland–Altman analyses, demonstrate the effectiveness of our approach for the extraction of biomarkers from AS-OCT images of the ciliary muscle. These results provide a more comprehensive evaluation of the accuracy and reliability of our approach for clinical applications.

Expanding on the quality of the obtained results, our proposed approach demonstrated good performance not only in quantitative analysis but also in qualitative analysis. Fig. 14 presents representative examples of the automatic extraction of biomarkers from 6 mm images, including the complete CMT profile representation with its perimeter and, illustrating the visually accurate and clinically interpretable results. It is important to note that the robustness of our approach was also tested with 16 mm images, and the results were similarly accurate, as shown in Fig. 15. These results highlight the potential of our approach to aid clinicians in accurately diagnosing and monitoring ocular diseases, ultimately improving patient outcomes.

4.3. Main limitations

Despite the good results achieves by our approach, there are some limitations. There is an inherent difficulty in achieving accurate measurements in this previously inaccessible area, even for expert examiners, given the challenges posed by pigmented tissues like the iris root and the lamina fusca, which obscure clear visualization due to light penetration limitations. This visualization issues can compromise the delineation of the studied structures, as well as the precise calculation of the biomarkers. Despite this challenges, our AS-OCT images offer high resolution. On the other hand, tissue refractive index distortion compensation was omitted, possibly impacting measurements of structures that deviate from the perpendicular to the AS-OCT optical axis. Additionally, no Laplace correction was applied, which could affect the accuracy of these measurements. In Fig. 16, we show two examples of results where the system does not perform an accurate segmentation. On the other hand, we used metrics bounded in intervals [0,1] and representing it with standard deviation can indeed imply non-feasible values. Regarding the biomarkers, the positioning of the posterior region to calculate the CML measure can be diffuse, favoring slightly imprecise measures.

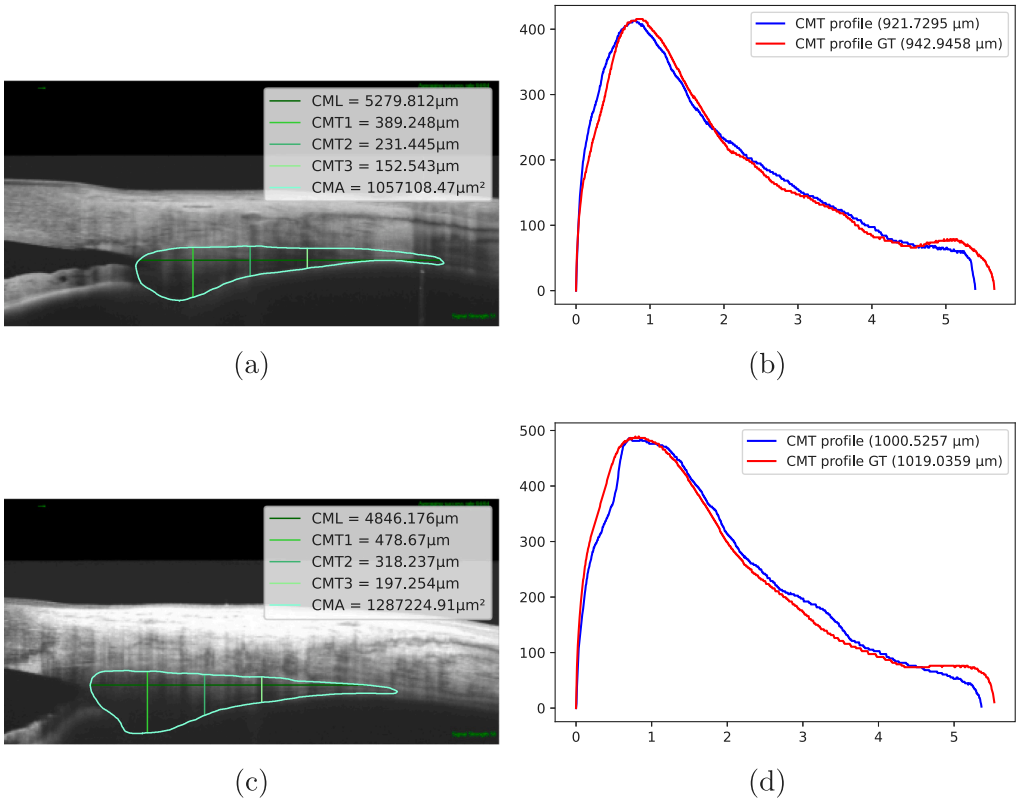

Fig. 14. Representative output examples of the automatic extraction of biomarkers in 6 mm images (a & c) and their CMT profile representations with their respective biomarkers (b & d).

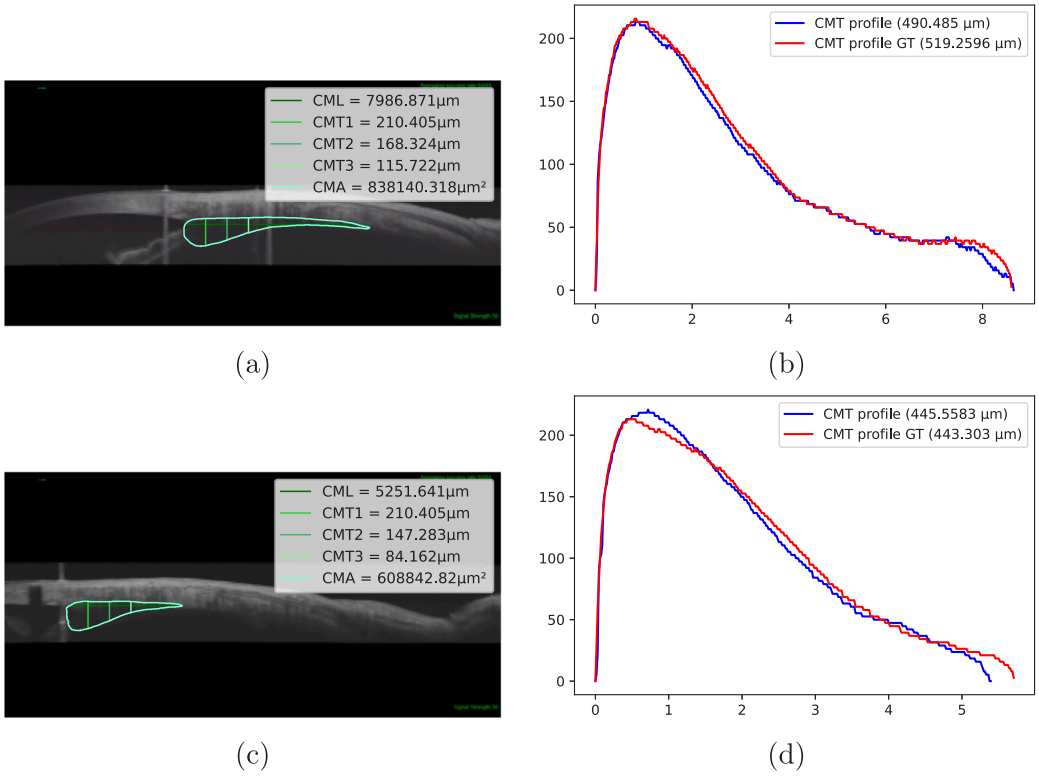

Fig. 15. Representative output examples of the automatic extraction of biomarkers in 16 mm images (a & c) and their CMT profile representations with their respective biomarkers (b & d).

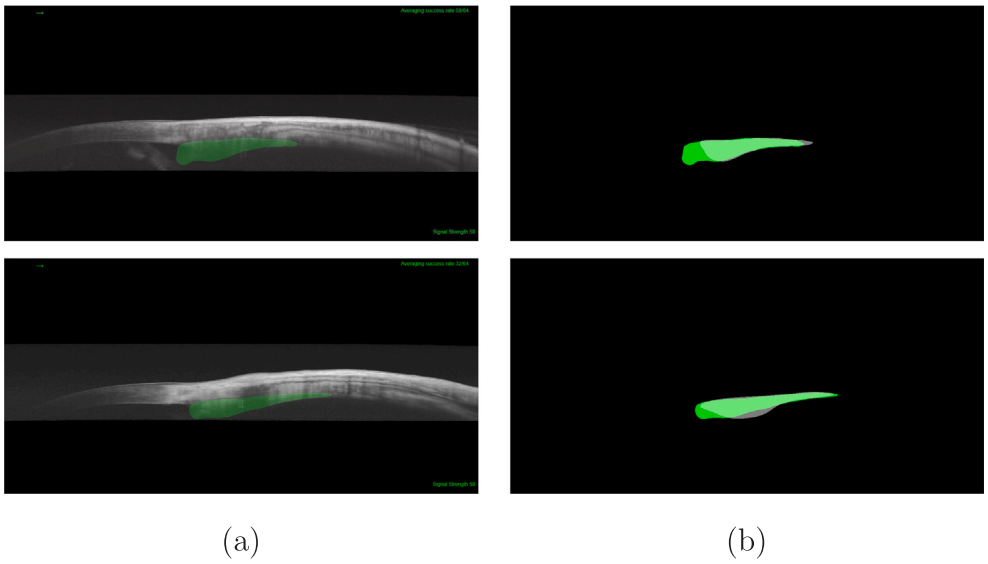

Fig. 16. Examples of the resulting bad segmented regions (green) in 6 mm images overlapped with: (a) the input image and (b) the manual label provided by a clinical expert (gray).

5. Conclusion

Our study presents a novel deep learning-based approach for automating the segmentation and extraction of biomarkers from AS-OCT images (6 mm and 16 mm) of the ciliary muscle. The results demonstrated the efficacy of our approach in achieving accurate segmentation of the ciliary muscle, as well as in the extraction of different computational biomarkers, considering the previously mentioned limitations. The proposed methodology has the potential to reduce the workload on clinical experts. Moreover, the results presented indicate that our approach is adaptable and can be extended to other types of AS-OCT images and biomarkers, potentially benefiting a broader range of clinical applications.

As future work, we plan to further refine our approach and potentially validate it against a dataset with the Posterior Limit of the ciliary muscle labeled to ascertain its efficacy and accuracy more comprehensively. Furthermore, integrating the tool into a web platform would enhance its accessibility and user-friendliness, potentially benefiting a broader range of clinicians and researchers. In addition, performing comparative clinical evaluations between normal and pathological conditions will enhance the validity and applicability of our findings in real-world clinical settings, fortifying the clinical implications of our work.

CRediT authorship contribution statement

Elena Goyanes: Methodology, Software, Validation, Writing – original draft, Visualization. **Joaquim de Moura:** Methodology, Software, Validation, Writing – review & editing, Visualization, Supervision. **José I. Fernández-Vigo:** Conceptualization, Data curation, Methodology, Supervision. **José A. Fernández-Vigo:** Data curation, Investigation, Methodology, Supervision. **Jorge Novo:** Conceptualization, Validation, Writing – review & editing, Supervision. **Marcos Ortega:** Conceptualization, Supervision, Project administration, Funding acquisition.

Declaration of competing interest

The authors declare that they have no known competing financial interests or personal relationships that could have appeared to influence the work reported in this paper.

Data availability

The authors do not have permission to share data.

Acknowledgments

This work was supported by Ministerio de Ciencia e Innovación, Government of Spain through the research project with [grant numbers RTI2018-095894-B-I00, PID2019-108435RB-I00, TED2021-131201B–I00, and PDC2022-133132-I00]; Consellería de Educación, Universidade, e Formación Profesional, Xunta de Galicia, Grupos de Referencia Competitiva, [grant number ED431C 2020/24]; predoctoral grant [grant number ED481A-2023-152]; CITIC, Centro de Investigación de Galicia [grant number ED431G 2019/01], receives financial support from Consellería de Educación, Universidade e Formación Profesional, Xunta de Galicia, through the ERDF (80%) and Secretaría Xeral de Universidades (20%). Funding for open access charge: Universidade da Coruña/CISUG.

References

[1] J.B. Jonas, R.A. Jonas, S.B. Jonas, S. Panda-Jonas, Ciliary body size in chronic angle-closure glaucoma, Sci. Rep. 13 (1) (2023) 16914.

[2] K.R.G. Aggarwala, Ocular accommodation, intraocular pressure, development of myopia and glaucoma: role of ciliary muscle, choroid and metabolism, Med. Hypothal. Discov. Innov. Ophthalmol. 9 (1) (2020) 66.

[3] R.V. Agrawal, S. Murthy, V. Sangwan, J. Biswas, Current approach in diagnosis and management of anterior uveitis, Indian J. Ophthalmol. 58 (1) (2010) 11.

[4] J. Gueudry, M. Muraine, Anterior uveitis, J. Francais d'Ophthalmol. 41 (1) (2018) e11–e21.

[5] J.C. Chen, K.L. Schmid, B. Brown, The autonomic control of accommodation and implications for human myopia development: a review, Ophthalmic Physiol. Opt. 23 (5) (2003) 401–422, http://dx.doi.org/10.1046/j.1475-1313.2003.00135.x, URL http://doi.wiley.com/10.1046/j.1475-1313.2003.00135.x.

[6] M.D. Bailey, L.T. Sinnott, D.O. Mutti, Ciliary body thickness and refractive error in children, Investig. Opthalmol. Vis. Sci. 49 (10) (2008) 4353, http://dx.doi.org/10.1167/iovs.08-2008, URL http://iovs.arvojournals.org/article.aspx?doi=10.1167/iovs.08-2008.

[7] A.L. Sheppard, L.N. Davies, In Vivo Analysis of Ciliary Muscle Morphologic Changes with Accommodation and Axial Ametropia, Invest. Ophthalmol. Vis. Sci. 51 (12) (2010) 6882–6889, http://dx.doi.org/10.1167/iovs.10-5787.

[8] L.A. Lossing, L.T. Sinnott, C.-Y. Kao, K. Richdale, M.D. Bailey, Measuring changes in ciliary muscle thickness with accommodation in Young adults, Optom. Vis. Sci. 89 (5) (2012) 719–726, http://dx.doi.org/10.1097/OPX.0b013e318252cadc, URL https://journals.lww.com/00006324-201205000-00023.

[9] H.A. Lewis, C.-Y. Kao, L.T. Sinnott, M.D. Bailey, Changes in ciliary muscle thickness during accommodation in Children, Optom. Vis. Sci. 89 (5) (2012) 727–737, http://dx.doi.org/10.1097/OPX.0b013e318253de7e, URL https://journals.lww.com/00006324-201205000-00024.

[10] H. Buckhurst, B. Gilmartin, R.P. Cubbidge, M. Nagra, N.S. Logan, Ocular biometric correlates of ciliary muscle thickness in human myopia, Ophthalmic Physiol. Opt. 33 (3) (2013) 294–304, http://dx.doi.org/10.1111/opo.12039, URL https://onlinelibrary.wiley.com/doi/10.1111/opo.12039.

[11] A.D. Pucker, L.T. Sinnott, C.-Y. Kao, M.D. Bailey, Region-specific relationships between refractive error and ciliary muscle thickness in children, Investig. Opthalmol. Vis. Sci. 54 (7) (2013) 4710, http://dx.doi.org/10.1167/iovs.13-11658, URL http://iovs.arvojournals.org/article.aspx?doi=10.1167/iovs.13-11658.

[12] M.K. Kuchem, L.T. Sinnott, C.-Y. Kao, M.D. Bailey, Ciliary muscle thickness in Anisometropia, Optom. Vis. Sci. 90 (11) (2013) 1312–1320, http://dx.doi.org/10.1097/OPX.0000000000000070, URL https://journals.lww.com/00006324-201311000-00021.

[13] J. Tabernero, E. Chirre, L. Hervella, P. Prieto, P. Artal, The accommodative ciliary muscle function is preserved in older humans, Sci. Rep. 6 (1) (2016) 25551.

[14] S. Wagner, E. Zrenner, T. Strasser, Ciliary muscle thickness profiles derived from optical coherence tomography images, Biomed. Opt. Express 9 (10) (2018) 5100, http://dx.doi.org/10.1364/BOE.9.005100, URL https://opg.optica.org/abstract.cfm?URI=boe-9-10-5100.

[15] S. Wagner, E. Zrenner, T. Strasser, Emmetropes and myopes differ little in their accommodation dynamics but strongly in their ciliary muscle morphology, Vis. Res. 163 (2019) 42–51, http://dx.doi.org/10.1016/j.visres.2019.08.002, URL https://linkinghub.elsevier.com/retrieve/pii/S0042698919301555.

[16] J.I. Fernández-Vigo, H. Shi, B. Kudsieh, P. Arriola-Villalobos, L. De-Pablo Gómez-de Liaño, J. García-Feijóo, J.Á. Fernández-Vigo, Ciliary muscle dimensions by swept-source optical coherence tomography and correlation study in a large population, Acta Ophthalmol. 98 (4) (2020) e487–e494, http://dx.doi.org/10.1111/aos.14304.

[17] J. Shi, J. Zhao, F. Zhao, R. Naidu, X. Zhou, Ciliary muscle morphology and accommodative lag in hyperopic anisometropic children, Int. Ophthalmol. 40 (917) (2020) 1573–2630, http://dx.doi.org/10.1007/s10792-019-01264-9.

[18] Z. Li, Z. Meng, W. Qu, X. Li, P. Chang, D. Wang, Y. Zhao, The Relationship Between Age and the Morphology of the Crystalline Lens, Ciliary Muscle, Trabecular Meshwork, and Schlemm's Canal: An in vivo Swept-Source Optical Coherence Tomography Study, Front. Physiol. 12 (2021) 763736, http://dx.doi.org/10.3389/fphys.2021.763736, URL https://www.frontiersin.org/articles/10.3389/fphys.2021.763736/full.

[19] X. Zhang, Q. Wu, T. Wen, H. Zhao, Q. Tian, J. Xu, G. Tang, R. Li, X. Guo, J. Song, H. Bi, In vivo analysis of ciliary muscle in myopic Chinese young adults using ArcScan Insight® 100, Ophthalmic Physiol. Opt. 42 (3) (2022) 559–570, http://dx.doi.org/10.1111/opo.12965, URL https://onlinelibrary.wiley.com/doi/10.1111/opo.12965.

[20] D. Kaphle, K.L. Schmid, L.N. Davies, M. Suheimat, D.A. Atchison, Ciliary Muscle Dimension Changes With Accommodation Vary in Myopia and Emmetropia, Invest. Ophthalmol. Vis. Sci. 63 (6) (2022) 24, http://dx.doi.org/10.1167/iovs.63.6.24.

[21] J. Ren, X. Gao, L. Chen, H. Lin, Y. Liu, Y. Zhou, Y. Liao, C. Xie, C. Zuo, M. Lin, Characteristics of the Ciliary Body in Healthy Chinese Subjects Evaluated by Radial and Transverse Imaging of Ultrasound Biometric Microscopy, J. Clin. Med. 11 (13) (2022) 3696, http://dx.doi.org/10.3390/jcm11133696, URL https://www.mdpi.com/2077-0383/11/13/3696.

[22] P. Cabaleiro, J. de Moura, J. Novo, P. Charlón, M. Ortega, Automatic identification and representation of the cornea–contact lens relationship using as-oct images, Sensors 19 (23) (2019) 5087.

[23] J.A. Izatt, Micrometer-scale resolution imaging of the anterior eye in vivo with optical coherence tomography, Arch. Ophthalmol. 112 (12) (1994) 1584, http://dx.doi.org/10.1001/archopht.1994.01090240090031.

[24] K. Gumus, C.H. Crockett, S.C. Pflugfelder, Anterior segment optical coherence tomography: a diagnostic instrument for conjunctivochalasis, Am. J. Ophthalmol. 150 (6) (2010) 798–806.

[25] W. Soliman, T.A. Mohamed, Spectral domain anterior segment optical coherence tomography assessment of pterygium and pinguecula, Acta Ophthalmol. 90 (5) (2012) 461–465.

[26] B.J. Thomas, A. Galor, A.A. Nanji, F. El Sayyad, J. Wang, S.R. Dubovy, M.G. Joag, C.L. Karp, Ultra high-resolution anterior segment optical coherence tomography in the diagnosis and management of ocular surface squamous neoplasia, Ocular Surf. 12 (1) (2014) 46–58.

[27] C.J. Pavlin, L.M. Vásquez, R. Lee, E.R. Simpson, I.I.K. Ahmed, Anterior segment optical coherence tomography and ultrasound biomicroscopy in the imaging of anterior segment tumors, Am. J. Ophthalmol. 147 (2) (2009) 214–219.

[28] A. Konstantopoulos, J. Kuo, D. Anderson, P. Hossain, Assessment of the use of anterior segment optical coherence tomography in microbial keratitis, Am. J. Ophthalmol. 146 (4) (2008) 534–542.

[29] A.O. Igbre, M.C. Rico, S.J. Garg, High-speed optical coherence tomography as a reliable adjuvant tool to grade ocular anterior chamber inflammation, Retina 34 (3) (2014) 504–508.

[30] E. Wylegala, D. Dobrowolski, A. Nowińska, D. Tarnawska, Anterior segment optical coherence tomography in eye injuries, Graefes Arch. Clin. Exp. 247 (2009) 451–455.

[31] A.L. Wong, C.K. Leung, R. Weinreb, A.K. Cheng, C.Y.L. Cheung, P.T. Lam, C.-P. Pang, D.S.C. Lam, Quantitative assessment of lens opacities with anterior segment optical coherence tomography, Br. J. Ophthalmol. 93 (1) (2009) 61–65.

[32] P. Nguyen, V. Chopra, Applications of optical coherence tomography in cataract surgery, Curr. Opin. Ophthalmol. 24 (1) (2013) 47–52.

[33] C.X. Qian, S. Hassanaly, M. Harissi-Dagher, Anterior segment optical coherence tomography in the long-term follow-up and detection of glaucoma in Boston type I keratoprosthesis, Ophthalmology 122 (2) (2015) 317–325.

[34] X. Xie, W. Sultan, G. Corradetti, J.Y. Lee, A. Song, A. Pardeshi, F. Yu, V. Chopra, S.R. Sadda, B.Y. Xu, et al., Assessing accommodative presbyopic biometric changes of the entire anterior segment using single swept-source OCT image acquisitions, Eye 36 (1) (2022) 119–128.

[35] O. Muftuoglu, B. Hosal, G. Zilelioglu, Ciliary body thickness in unilateral high axial myopia, Eye 23 (5) (2009) 1176–1181.

[36] S. Wagner, E. Süer, B. Sigdel, E. Zrenner, T. Strasser, Monocular transcorneal electrical stimulation induces ciliary muscle thickening in contralateral eye, Exp. Eye Res. 231 (2023) 109475.

[37] E. Owusu, N.M. Shasteen, G.L. Mitchell, M.D. Bailey, C.-Y. Kao, A.J. Toole, K. Richdale, M.T. Kulp, Impact of accommodative insufficiency and accommodative/vergence therapy on ciliary muscle thickness in the eye, Ophthalmic Physiol. Opt. (2023).

[38] C.-Y. Kao, K. Richdale, L.T. Sinnott, L.E. Grillott, M.D. Bailey, Semiautomatic Extraction Algorithm for Images of the Ciliary Muscle, Optom. Vis. Sci. 88 (2) (2011) 275–289, http://dx.doi.org/10.1097/OPX.0b013e3182044b94, URL https://journals.lww.com/00006324-201102000-00015.

[39] M. Ruggeri, V. Hernandez, C. de Freitas, F. Manns, J.-M. Parel, Biometry of the ciliary muscle during dynamic accommodation assessed with OCT, in: F. Manns, P.G. Söderberg, A. Ho (Eds.), Ophthalmic Technologies XXIV, Vol. 8930, SPIE,International Society for Optics and Photonics, 2014, pp. 140–146, http://dx.doi.org/10.1117/12.2044309.

[40] D.S. Laughton, B.J. Coldrick, A.L. Sheppard, L.N. Davies, A program to analyse optical coherence tomography images of the ciliary muscle, Contact Lens Anterior Eye 38 (6) (2015) 402–408, http://dx.doi.org/10.1016/j.clae.2015.05.007, URL https://www.sciencedirect.com/science/article/pii/S1367048415000831.

[41] T. Straßer, S. Wagner, E. Zrenner, Review of the application of the open-source software ciloct for semi-automatic segmentation and analysis of the ciliary muscle in oct images, PLoS One 15 (6) (2020) 1–10, http://dx.doi.org/10.1371/journal.pone.0234330.

[42] E. Goyanes, J. de Moura, J. Novo, J.I. Fernández-Vigo, J.Á. Fernández-Vigo, M. Ortega, Fully-automatic segmentation of the ciliary muscle using anterior segment optical coherence tomography images, in: 2022 International Joint Conference on Neural Networks, IJCNN, 2022, http://dx.doi.org/10.1109/IJCNN55064.2022.9892316.

[43] I. Cabeza-Gil, M. Ruggeri, Y.-C. Chang, B. Calvo, F. Manns, Automated segmentation of the ciliary muscle in OCT images using fully convolutional networks, Biomed. Opt. Express 13 (5) (2022) 2810—2823, http://dx.doi.org/10.1364/boe.455661.

[44] T. Straß er, S. Wagner, Performance of the deep neural network ciloctunet, integrated with open-source software for ciliary muscle segmentation in anterior segment OCT images, is on par with experienced examiners, Diagnostics 12 (12) (2022) 3055.

[45] W. Chen, X. Yu, Y. Ye, H. Gao, X. Cao, G. Lin, R. Zhang, Z. Li, X. Wang, Y. Zhou, et al., CMS-NET: deep learning algorithm to segment and quantify the ciliary muscle in swept-source optical coherence tomography images, Ther. Adv. Chronic Dis. 14 (2023) 20406223231159616.

[46] P. Yakubovskiy, Segmentation models pytorch, in: GitHub Repository, 2020, GitHub, URL https://github.com/qubvel/segmentation_models.pytorch.

[47] O. Ronneberger, P. Fischer, T. Brox, U-net: Convolutional networks for biomedical image segmentation, in: International Conference on Medical Image Computing and Computer-Assisted Intervention, Springer, 2015, pp. 234–241, http://dx.doi.org/10.1007/978-3-319-24574-4_28.

[48] T.-Y. Lin, P. Dollar, R. Girshick, K. He, B. Hariharan, S. Belongie, Feature pyramid networks for object detection, in: 2017 IEEE Conference on Computer Vision and Pattern Recognition, CVPR, 2017, http://dx.doi.org/10.1109/cvpr.2017.106.

[49] M. Gende, J. de Moura, J. Novo, M. Ortega, End-to-end multi-task learning approaches for the joint epiretinal membrane segmentation and screening in OCT images, Comput. Med. Imaging Graph. 98 (2022) 102068.

[50] J. Le'Clerc Arrastia, N. Heilenkötter, D. Otero Baguer, L. Hauberg-Lotte, T. Boskamp, S. Hetzer, N. Duschner, J. Schaller, P. Maass, Deeply supervised unet for semantic segmentation to assist dermatopathological assessment of basal cell carcinoma, J. Imaging 7 (4) (2021) 71.

[51] D. Sarwinda, R.H. Paradisa, A. Bustamam, P. Anggia, Deep learning in image classification using residual network (ResNet) variants for detection of colorectal cancer, Procedia Comput. Sci. 179 (2021) 423–431.

[52] K.Y. Foo, K. Newman, Q. Fang, P. Gong, H.M. Ismail, D.D. Lakhiani, R. Zilkens, B.F. Dessauvagie, B. Latham, C.M. Saunders, et al., Multi-class classification of breast tissue using optical coherence tomography and attenuation imaging combined via deep learning, Biomed. Opt. Express 13 (6) (2022) 3380–3400.

[53] N.H. Ali, A.R. Abdullah, N.M. Saad, A.S. Muda, Collateral circulation classification based on cone beam computed tomography images using ResNet18 convolutional neural network.

[54] M. Talo, U.B. Baloglu, Ö. Yıldırım, U.R. Acharya, Application of deep transfer learning for automated brain abnormality classification using MR images, Cogn. Syst. Res. 54 (2019) 176–188.

[55] S.Q. Nisa, A.R. Ismail, Dual U-net with resnet encoder for segmentation of medical images, Int. J. Adv. Comput. Sci. Appl. 13 (12) (2022).

[56] K. He, X. Zhang, S. Ren, J. Sun, Deep residual learning for image recognition, in: Proceedings of the IEEE Conference on Computer Vision and Pattern Recognition, 2016, pp. 770–778, http://dx.doi.org/10.1109/CVPR.2016.90, URL https://ieeexplore.ieee.org/document/7780459.

[57] D.P. Kingma, J. Ba, Adam: A method for stochastic optimization, 2014, arXiv preprint arXiv:1412.6980.

[58] K. Simonyan, A. Zisserman, Very deep convolutional networks for large-scale image recognition, 2014, arXiv preprint arXiv:1409.1556.

[59] J. de Moura, J. Novo, M. Ortega, N. Barreira, M.G. Penedo, Automated segmentation of the central serous chorioretinopathy fluid regions using optical coherence tomography scans, in: 2021 IEEE 34th International Symposium on Computer-Based Medical Systems, CBMS, IEEE, 2021, pp. 1–6, http://dx.doi.org/10.1109/CBMS52027.2021.000104, URL https://ieeexplore.ieee.org/document/9474709.

[60] G. Samagaio, J. de Moura, J. Novo, M. Ortega, Automatic segmentation of diffuse retinal thickening edemas using optical coherence tomography images, Procedia Comput. Sci. 126 (2018) 472–481, http://dx.doi.org/10.1016/j.procs.2018.07.281.

[61] H.A. Anderson, M.D. Bailey, R.E. Manny, C.-Y. Kao, Ciliary muscle thickness in adults with Down syndrome, Ophthalmic Physiol. Opt. 42 (4) (2022) 897–903, http://dx.doi.org/10.1111/opo.12974, URL https://onlinelibrary.wiley.com/doi/10.1111/opo.12974.

[62] A. Domínguez-Vicent, D. Monsálvez-Romín, J.J. Esteve-Taboada, R. Montés-Micó, T. Ferrer-Blasco, Effect of age in the ciliary muscle during accommodation: Sectorial analysis, J. Optom. 12 (1) (2019) 14–21, http://dx.doi.org/10.1016/j.optom.2018.01.001, URL https://www.sciencedirect.com/science/article/pii/S1888429618300025.

[63] D. Monsálvez-Romín, A. Domínguez-Vicent, J.J. Esteve-Taboada, R. Montés-Micó, T. Ferrer-Blasco, Multisectorial changes in the ciliary muscle during accommodation measured with high-resolution optical coherence tomography, Arq. Bras. Oftalmol. 82 (3) (2019) 207–213.

[64] M. Ang, W. Chong, H. Huang, W.T. Tay, T.Y. Wong, M.-G. He, T. Aung, J.S. Mehta, Comparison of anterior segment optical tomography parameters measured using a semi-automatic software to standard clinical instruments, PLoS One 8 (6) (2013) e65559.

[65] X.-F. Zhang, M. Li, Y. Shi, X.-H. Wan, H.-Z. Wang, Repeatability and agreement of two anterior segment OCT in myopic patients before implantable collamer lenses implantation, Int. J. Ophthalmol. 13 (4) (2020) 625.

[66] Y. Du, C. Jin, S. Yin, G. Wang, Q. Ma, Y. Li, B. Chen, H. Wang, K. Qiu, M. Zhang, Comparison of vault measurements using a swept-source OCT-based optical biometer and anterior segment OCT, Front. Med. 9 (2022) 865719.

[67] P.S. Zhao, T.Y. Wong, W.-L. Wong, S.-M. Saw, T. Aung, Comparison of central corneal thickness measurements by visante anterior segment optical coherence tomography with ultrasound pachymetry, Am. J. Ophthalmol. 143 (6) (2007) 1047–1049.